A variable near-infrared counterpart to the neutron-star low-mass X-ray binary 4U 1705−440[1]

Jeroen Homan, David L. Kaplan[2]

MIT Kavli Institute for Astrophysics and Space Research, 70 Vassar Street, Cambridge, MA 02139
jeroen@space.mit.edu,dlk@space.mit.edu

Maureen van den Berg

Harvard-Smithsonian Center for Astrophysics, Cambridge, MA 02138
maureen@head.cfa.harvard.edu

and

Andrew J. Young

Astrophysics Group, Department of Physics, Bristol University, Bristol, BS8 1TL, UK
andy.young@bristol.ac.uk

ABSTRACT

We report the discovery of a near-infrared (nIR) counterpart to the persistent neutron-star low-mass X-ray binary 4U 1705−440, at a location consistent with its recently determined *Chandra* X-ray position. The nIR source is highly variable, with K_s-band magnitudes varying between 15.2 and 17.3 and additional J- and H-band observations revealing color variations. A comparison with contemporaneous X-ray monitoring observations shows that the nIR brightness correlates well with X-ray flux and X-ray spectral state. We also find possible indications for a change in the slope of the nIR/X-ray flux relation between different X-ray states. We discuss and test various proposed mechanisms for the nIR emission from neutron-star low-mass X-ray binaries and conclude that the nIR emission in 4U 1705−440 is most likely dominated by X-ray heating of the outer accretion disk and the secondary star.

Subject headings: accretion, accretion disks — binaries: close — stars: individual (4U 1705−440) — X-rays: binaries

---

[1]This paper includes data gathered with the 6.5 meter Magellan Baade Telescope located at Las Campanas Observatory, Chile, and the 4 meter Blanco Telescope located at CTIO, Chile.

[2]MIT Pappalardo and Hubble Fellow

1. Introduction

4U 1705−440 is a neutron-star low-mass X-ray binary (NSXB) that was discovered in the early 1970's with the Uhuru satellite (Giacconi et al. 1972). The X-ray spectral and variability properties place it among the class of the so-called atoll sources (Hasinger & van der Klis 1989), persistent NSXBs that accrete between a few and a few tens of percents of the Eddington luminosity. The source shows type-I (thermonuclear) X-ray bursts (Sztajno et al. 1985; Gottwald et al. 1989), strong rapid variability (Olive et al. 2003), including kHz quasi-periodic oscillations (Ford et al. 1998), and some of the strongest long-term X-ray variations seen in persistent NSXBs (Reig et al. 2003). These long-term variations correspond to X-ray spectral-state transitions, as was shown by Barret & Olive (2002).

Despite the fact that 4U 1705−440 has been known for more than 35 years, no optical, infrared, or radio counterparts have been identified. Given the pronounced X-ray state transitions and large luminosity changes in 4U 1705−440, such counterparts are expected to be variable as well, which should in principle facilitate identification efforts. The main reason that counterparts have not been found is that, until recently, no accurate X-ray source position was available, impeding identification efforts in the crowded Galactic-bulge field. This changed with a *Chandra* observation by di Salvo et al. (2005), which yielded source coordinates with an absolute uncertainty of $\sim 0\farcs5$. As noted by di Salvo et al. (2005), these new coordinates differ significantly from previously reported ones, by $\sim 0\farcm15$.

We have conducted a search for the near-infrared (nIR) counterpart of 4U 1705−440, taking advantage of the improved *Chandra* position. The main benefit of searching in the nIR in comparison to the optical is the much lower extinction; based on N_H estimates from X-ray spectra (Piraino et al. 2007) we expect $A_V \approx 10.8$, but only $A_K \approx 1.3$. Moreover, as was recently shown by Russell et al. (2006, 2007), the nIR can provide important constraints on the emission properties of the jet and accretion disk in NSXBs. In particular, for atoll sources Russell et al. (2007) found that above an X-ray luminosity of 10^{36} erg s^{-1} the nIR is dominated by jet emission, while below these luminosities X-ray reprocessing in the accretion disk dominates (although thermal emission from the disk cannot be ruled out).

In this paper we report the discovery of a variable nIR counterpart to 4U 1705−440. In §2 we present our nIR observations along with a set of quasi-simultaneous X-ray observations. The identification of the nIR counterpart and a study of nIR/X-ray correlations are presented in §3. Finally, in §4, we discuss our results in the framework of several proposed mechanisms for nIR emission in NSXBs.

2. Observations & Data Reduction

2.1. near-Infrared

We observed the field of 4U 1705−440 a number of times in the nIR between 2006 May 16 and 2007 September 22. Our primary observations were with the 6.5 m Magellan I (Baade) telescope and Persson's Auxiliary Nasmyth Infrared Camera (PANIC; Martini et al. 2004), which contains a 1024×1024 HAWAII I HgCdTe detector with a $0\farcs125$ plate scale for a $128'' \times 128''$ field of view. We also obtained two observations with the 4 m Blanco Telescope at the Cerro Tololo Inter-American Observatory (CTIO), using the Infrared Side Port Imager (ISPI). ISPI has a 2048×2048 HgCdTe HAWAII-2 array with $0\farcs3$ plate scale, for a $10\farcm25 \times 10\farcm25$ field of view, although to match the PANIC data and to avoid dealing with geometric distortions we only used the central 512×512 pixels. The majority of the data were taken with a $K_{\rm s}$ filter, but we did obtain some observations with the J and H filters. A log of the observations is given in Table 1. There we list the total exposure times for each observation, although the data actually consist of a number of short (10–20 s for $K_{\rm s}$, and up to 48 s for the other filters) exposures taken at positions dithered by up to $10''$.

We reduced the data using custom routines in `PyRAF`. First we linearized the data using the coefficients given on the PANIC[3] and ISPI[4] web sites. We then subtracted dark frames, divided by a flat field (using twilight flats for PANIC and dome flats for ISPI), and then produced a sky frame for subtraction by averaging the four exposures on either side of a given exposure. We then added the sky-subtracted exposures together, identified all the stars, and produced masks for the stars to improve the sky frames in a second round of sky subtraction. The coaddition of the individual exposures shifted the images of all the bands from a given observation to the same position.

For a reference observation, we used Epoch 1 from Table 1 (2006 May 16). We determined the astrometry using 64 2MASS (Skrutskie et al. 2006) stars that were well isolated and not very saturated, fitting for a plate scale, rotation, and zero point. The solution for the $K_{\rm s}$ image had an rms of $0\farcs07$ in each coordinate, and we transferred that solution to the other bands. For photometry, we used 34 2MASS stars that were unsaturated in all bands, well detected in 2MASS, and well isolated in all the data. We determined a zero point for each band (not including any color terms), and got zero-point uncertainties of 0.09 mag.

All of the other data were corrected to the astrometry and photometry of Epoch 1.

[3] `http://www.lco.cl/lco/telescopes-information/magellan/instruments-1/panic/panic-documentation/panic-`

[4] `http://www.ctio.noao.edu/instruments/ir_instruments/ispi/New/UsersGuide/linearity.html`.

A list of star positions and magnitudes for 820 stars that were well-detected was produced by running `sextractor` (Bertin & Arnouts 1996) on the stacked images of each band of Epoch 1. We then ran `sextractor` to measure each of those stars in all of the other PANIC images. To compute the astrometric solution we used about 450 stars in each K_s exposure and got rms residuals of $\approx 0\farcs03$ in each coordinate. We then transferred the solutions to the J and H bands. The photometric referencing was done using 16 stars within $40''$ and ± 2 mag of 4U 1705−440 (based on the 2006 May 16 observation; see below), shown in Figure 1. We selected these stars by searching through the 820 initially identified stars for those with the lowest variation between all of the exposures, after correcting for different zero points. These stars had rms variations of < 0.05 mag over all the K_s observations.

2.2. X-rays

During part of the period in which the nIR observations of 4U 1705−440 were done, the source was monitored in X-rays with a number of instruments. For this paper we made use of publicly available data from the All-Sky Monitor[5] (ASM; Levine et al. 1996) on-board the *Rossi X-ray Timing Explorer* (*RXTE*) and the *Swift* Burst Alert Telescope[6] (BAT; Barthelmy et al. 2005). The ASM and BAT typically observed the source a few times per day in the 2–10 keV and 15–150 keV bands, respectively. In the period between 2007 Aug 11 and 2007 Sep 11 no BAT data were available due to attitude control problems on the *Swift* spacecraft

Additional X-ray data from pointed observations with the Proportional Counter Array (PCA; Jahoda et al. 2006) and High Energy X-ray Timing Experiment (HEXTE; Rothschild et al. 1998) onboard *RXTE* were analyzed. These instruments provide coverage in the 2–60 keV and 15–250 keV bands, respectively. Starting from 2007 June 26 we observed 4U 1705−440 on average once every four days. The PCA and HEXTE data were analyzed with FTOOLS V6.3. We obtained background-corrected count rates from the PCA and HEXTE in energy bands that closely match the energy bands of the ASM and BAT: 3–10 keV for the PCA and 15–150 keV for HEXTE.

The PCA and HEXTE data were also used for a spectral analysis. For the data reduction and modeling of the spectra we followed the data-reduction and analysis steps taken by Lin et al. (2007). Spectral fits were made in the 3.5–150 keV band, with the N_H fixed to

[5]http://xte.mit.edu/ASM_lc.html

[6]http://heasarc.gsfc.nasa.gov/docs/swift/results/transients/

1.9×10^{22} atoms cm^{-2} (Piraino et al. 2007).

3. Results

3.1. Near-Infrared Counterpart Identification

Examining our Epoch 1 data, we find a single bright object within the *Chandra* error circle (J2000): $\alpha = 17^{\rm h}08^{\rm m}54\overset{\rm s}{.}47$, $\delta = -44°06'07\overset{''}{.}4$, with an uncertainty (90%) of $0\overset{''}{.}6$ determined by the *Chandra* absolute pointing uncertainty (see Fig. 1). This nIR source, at $\alpha = 17^{\rm h}08^{\rm m}54\overset{\rm s}{.}48$, $\delta = -44°06'07\overset{''}{.}4$, is well within the *Chandra* error circle, and is consistent with an unresolved point source in all of the data. In the Epoch 1 observations, this source has $K_{\rm s} = 15.23 \pm 0.02$, $H = 16.03 \pm 0.02$, and $J = 17.14 \pm 0.02$, where the errors only reflect the measurement uncertainties.

When comparing all observations, it becomes apparent that the source varies considerably. These variations are not caused by the different seeing conditions. In Figure 2 we plot all our photometric data, with the photometry listed in Table 2. Uncertainties of ∼0.05 mag arising from our flat-fielding and sky-subtraction procedures were not included in the Table, but were taken into account in all figures. We include the two best comparison stars in Figure 2, which have rms brightness variations of < 0.06 mag. In the K_s-band, in which we have the most observations, the counterpart varies by as much as 2 mag. Similar variations are seen in the other bands, although there are considerable color variations; $H - K_s$ varies by ∼0.4 and $J - K_s$ by ∼0.6. These color changes appear to be uncorrelated to changes in nIR brightness. In Figure 3 we plot a few representative nIR spectral energy distributions. The data for the spectral energy distributions were de-reddened assuming an N_H of 1.9×10^{22} atoms cm^{-2} (Piraino et al. 2007), which was converted to various reddening factors at particular wavelengths, following Predehl & Schmitt (1995), Cardelli et al. (1989), and Dutra et al. (2002): $A_{K_s} = 1.27$, $A_H = 2.04$, and $A_J = 3.03$. A comparison with the slopes of disk and jet spectra, which are also shown in Figure 3, seems to rule out significant optically thin jet emission in the nIR (see also §4) .

3.2. Near-Infrared/X-ray correlations

The X-ray light curves from the ASM (one-day averages), the BAT (four-day averages), and PCA/HEXTE (single observation averages) are shown in Figure 4. The times of the nIR observations are indicated in the panel with ASM data and the corresponding nIR epoch numbers are given on top. The X-ray state-transition cycles can clearly be seen, with the

15–150 keV count rates increasing during periods of low 2–10 keV flux. The nIR properties of 4U 1705−440 were studied as a function of X-ray flux and as a function of position in X-ray color diagrams.

3.2.1. X-ray fluxes

For the X-ray flux study we only made use of PCA and HEXTE data, since the ASM and BAT data are not suitable for spectral fitting. We only used PCA/HEXTE data that were taken within two days of our nIR observations; this resulted in 10 observations, two of which were combined (for nIR Epoch 10). The PCA and HEXTE spectra were fit in XSPEC V11.3 (Arnaud 1996) with simple phenomenological models (Lin et al. 2007). For spectrally-hard observations this model consisted of a black body, to represent the boundary layer between the disk and neutron star, and a broken power law, for the non-thermal emission. For spectrally-soft spectra an additional disk black body was needed, to fit the accretion disk component. The models also included an absorption component that was fixed at 1.9×10^{22} atoms cm^{-2}. These models resulted in good fits for all our observations. Unabsorbed 3–100 keV fluxes were extracted and in Figure 5 we plot the K_s-band flux density versus the 3–100 keV X-ray flux; error bars for the X-ray fluxes were set at 5%. A clear, positive correlation can be seen; fits with a power law resulted in a nIR/X-ray slope of 0.66±0.02 (see dashed line in Fig. 5). Separating the data based on relative strength of the thermal (blackbody and disk black body) and non-thermal (power-law) components in the X-ray spectrum, suggests that the nIR/X-ray flux relation is considerably steeper for non-thermal dominated (3-100 keV flux contribution $> 75\%$) X-ray spectra (1.33±0.11; open squares) than in the thermal dominated ($> 85\%$) ones (0.37±0.03; filled circles), however, we note that the number of points in both selections is small and that the non-thermal data points span a very narrow range in X-ray flux. We also point out that the low energy boundary of 3 keV means that a large fraction of the flux falls outside our flux band, especially for the soft spectra.

3.2.2. X-ray color diagrams

Spectral states of NSXBs are often studied in terms of color-color or color-intensity diagrams. Since the count rates from the ASM, BAT, and HEXTE were often too low to produce reliable colors from them, our diagrams were created from PCA data only. The PCA data were supplemented by publicly available data of 4U 1705−440 from *RXTE* observation cycles 9 and 10 (February 2004 until November 2006), allowing us to put our own observations in a better context. The color-color and color-intensity diagrams are shown in Figure 6,

in which we also identify the spectrally-hard ("extreme island"), transitional ("island"), and soft ("banana") states (Lin et al. 2007; van der Klis 2006). These spectral states appear as well-separated branches in the color-color diagram. Since only nine of our nIR observations could be matched with PCA data we explored an alternative way to identify spectral states that could also be applied to the ASM, BAT, and HEXTE data of 4U 1705−440. As a solution we simply plotted count rates from a low energy band (∼2–10 keV) versus count rates from a high energy band (∼15-150 keV). This was done for the ASM and BAT four-day averaged count rates and separately for our PCA and HEXTE data. To allow comparison between the ASM/BAT and PCA/HEXTE count-rate diagrams, the count rates of the various instruments were renormalized. First, the ASM and BAT count rates were scaled by their maximum four-day averaged values (from at least 3σ detections) from the period after the start of the BAT coverage (25.6 counts s^{-1} and 2.1×10^{-2} counts s^{-1}, respectively). The scaling factors for the PCA and HEXTE light curves were determined visually by finding the best overlap with the renormalized ASM and BAT light curves, resulting in scaling factors of 869 counts s^{-1} for the PCA and 17.4 counts s^{-1} for HEXTE. The scaled ASM/BAT and PCA/HEXTE count rate diagrams are shown in Figure 7. Both the ASM/BAT and PCA/HEXTE diagrams reveal similar two branched structures. The symbols/colors for the PCA/HEXTE panel are the same as for Figure 6 and a comparison with that figure shows that the left-side branch corresponds to the spectrally-hard ("extreme island") state and the right-side branch corresponds to the soft ("banana") state. The transitional ("island") state is not well separated in these diagrams, largely overlapping with the hard state branch. Note that the branches of the ASM/BAT track are slightly shorter than those from PCA/HEXTE, mainly because of missing *Swift* data in the August/September 2007 period.

To understand how the broadband X-ray flux changed along the tracks in Figure 7 we fitted the spectra of all the PCA/HEXTE observations in that figure (109 in total) using the same model as above and obtained unabsorbed fluxes in the 0.5–100 keV band, by extrapolating well below our low-energy boundary. The main reason for extrapolating down to 0.5 keV was to capture more flux from the thermal components, although uncertainties are involved in extrapolating to such low energies. We found that on the spectrally-hard branch the 0.5-100 keV flux correlated well with the HEXTE count rate and that on the spectrally soft branch the 0.5-100 keV flux correlated well with the PCA count rate. This suggests that mass-accretion rate increases as the source moves up either branch. The 0.5-100 keV flux range observed on the hard branch was $1.1\text{–}8.5\times10^{-9}$ erg s^{-1} cm^{-2}; on the soft branch we measured $1.8\text{–}24\times10^{-9}$ erg s^{-1} cm^{-2}. Considering only the ten X-ray observations that were associated with the nIR observations, we find that the ones on the spectrally-soft branch all had higher 0.5–100 keV fluxes that the ones on the spectrally-hard branch.

Using the same PCA observations as for our spectral analysis (§3.2.1), we overplot the

nIR data (grey circles) in the color-color and color-intensity diagrams in Figure 6, with the size of the symbols scaling linearly with the nIR flux density. Clearly, the brightest nIR observations occurred in the spectrally-soft state, in which the X-ray flux reaches its maximum. We also selected ASM/BAT data that were closest in time to our nIR observations, using three- or four-day ASM/BAT averages that were centered on the times nIR observations. These data are plotted in Figure 7, together with the PCA/HEXTE data (for which we used the same nIR/X-ray combinations as for Figures 5 and 6). Clearly, a large part of the full X-ray spectral range was covered by our nIR observations. The locations of the nIR epochs that were covered by ASM/BAT as well as PCA/HEXTE observations were consistent between the two diagrams, except for Epoch 18, for which we derived a scaled ASM count rate of 0.96(3) counts s^{-1}, but a scaled PCA count rate of 1.13(1) counts s^{-1}. As can be seen from Figure 7, the additional ASM/BAT data strengthen our initial finding from Figure 6 that nIR fluxes are highest in the spectrally-soft state. In Table 2 we have listed the spectral branch on which each of the nIR observations occurred; two observations occurred near the vertex of the two branches and identification is therefore uncertain. Comparison of Figure 7 and Table 2 shows that all soft-state observations have higher nIR fluxes than the hard-state observations. Since this is also true for the X-ray fluxes, the spectral-state dependence of the nIR flux might therefore simply reflect the nIR dependence on X-ray flux (see also §4).

4. Discussion and conclusions

We have made nIR observations of the field of the NSXB 4U 1705−440 and discovered a variable counterpart at the location of the *Chandra* X-ray source. The K_s-band magnitude varied between 15.2 and 17.3 and additional J- and H-band observations revealed color changes that did not correlate with nIR brightness variations. Using 18 epochs of nIR observations in combination with X-ray monitoring observations, we were able to study, for the first time, the nIR changes along an atoll color-color track. We found that 4U 1705−440 has a significantly higher nIR flux in the spectrally-soft ("banana") state than in the spectrally-hard ("extreme-island") state, although this might simply be the result of the higher X-ray fluxes (and mass-accretion rates) in the former state. The nIR flux density correlated well with X-ray flux, with possible indications for a steeper dependence in the spectrally-hard state.

Comparing the monochromatic nIR luminosity of 4U 1705−440 ($\log(L_{K_s}) \sim 19.2-20.0$ [7.2 kpc], $\sim 19.5-20.3$ [9.6 kpc]; for distance estimates, see below) with that of other NSXBs published in Russell et al. (2007), we find values that are very similar to systems with comparable X-ray luminosities. For $F_{3-100\,keV}/F_{K_s}$ we find values of 1.4–4.4×10^3. Russell et al.

(2006, 2007) discussed possible mechanisms for the nIR emission in NSXBs: optically-thin emission from the inner regions of a jet outflow close to the neutron star, thermal emission from an X-ray or viscously-heated disk, or thermal emission from the companion star. X-ray heating of the secondary was not explicitly considered by Russell et al. (2006, 2007), even though it can be a significant source of optical emission, as shown by Zurita et al. (2000), and presumably also of nIR emission. However, since it is difficult to distinguish heating of the disk from heating of the secondary with our data, we will not discuss the latter option separately.

We start with an assessment of the contribution from a non-heated secondary star. The mass donors in low-mass X-ray binaries are typically late-type dwarfs or giants. We compare the absolute K_s magnitudes of 4U 1705−440 with published K values for K4 and M4 dwarfs, and K5 and M5 giants (Bessell & Brett 1988; Bessell 1991; Mikami & Heck 1982; Carroll & Ostlie 1996), calculated using the distance estimates derived at the end of this section and a correction for absorption that is based on an N_H of $1.9{\times}10^{22}$ atoms cm^{-2}. For dwarfs we find that they are three to seven magnitudes fainter than our lowest observed values. The absolute magnitudes of the giants, on the other hand, are three to four magnitudes brighter than our highest observed values. Note that these comparisons suffer from considerable distance and reddening related uncertainties. Nevertheless, these findings, in combination with the amplitude of the nIR variations, appear to rule out that thermal emission from a non-heated late-type dwarf or giant dominates the nIR emission of 4U 1705−440. Given that the expected nIR emission from giants is higher than what we observe, the secondary in 4U 1705−440 is most likely a dwarf. This would then imply an orbital period of ∼1–10 hrs for a Roche-lobe filling primary, which needs to be tested with follow-up photometry.

To distinguish between the other possible mechanisms that are listed above, Russell et al. (2006, 2007) employed nIR/X-ray luminosity correlations and spectral energy distributions. In Figure 3 we compare the nIR spectral energy distributions of 4U 1705−440 with models for optically-thin jet synchrotron emission ($\propto \nu^{-0.6}$; average slope taken from Fender 2006, solid grey line), the Rayleigh-Jeans tail of a multi-color disk black-body spectrum ($\propto \nu^{2}$; Frank et al. 1992, dashed line) and the $\nu^{1/3}$ slope of a multi-color disk spectrum that is characteristic for frequencies higher than the Rayleigh-Jeans part (dotted line). The frequency of the break between the ν^2 and $\nu^{1/3}$ slopes of a multi-color disk black-body increases with mass-accretion rate and decreases with the size of the accretion disk. Slopes for an X-ray-heated accretion disk are not included in Figure 3. Such heating results in an additional bump in the optical/UV (Vrtilek et al. 1990) and also extends the high-frequency end of the Rayleigh-Jeans tail to higher frequencies. Based on the model slopes in Figure 3, a significant contribution to the nIR from optically-thin jet synchrotron emission can be ruled

out; the slope of the nIR spectrum is the opposite of that expected from a jet and the relatively small changes in the shape of the spectrum also rule out significant changes in the nIR contribution from a jet across the observed nIR luminosity range. Recent *Spitzer* observations of another atoll source NSXB, 4U 0614+091, by Migliari et al. (2006), suggest that one has to observe at lower IR frequencies to detect clear spectral signatures from a jet in NSXBs. In that source the jet synchrotron emission had a slope of -0.57, indicative of optically-thin emission and close to the -0.6 slope we adopted in Figure 3. The dependence of nIR flux on X-ray spectral state also argues against a jet interpretation of the nIR flux. Observations of black-hole LMXBs (Homan et al. 2005; Buxton & Bailyn 2004) have shown that the nIR contribution from a jet changes significantly during transitions between spectrally-hard and soft X-ray states, with the nIR contribution in hard states being higher. In 4U 1705−440 we observe the opposite behavior, suggesting that the nIR flux is dominated by other components.

The slopes of the spectral energy distributions in Figure 3 are consistent with those of multi-color disk black body models, being closer the Rayleigh-Jeans tail on the low-frequency end and closer to the flatter part of a disk spectrum on the high-frequency end. We note that in recent literature on 4U 1705−440 N_H values in the range of 1.2–2.4$\times10^{22}$ atoms cm^{-2} can be found (we adopted 1.9$\times10^{22}$ atoms cm^{-2}). The low value of this range brings the slope closer to that of the flat part of a disk spectrum, but still far from the jet slope, whereas the high value steepens the data to bring them closer to the slope of the Rayleigh-Jeans tail. Based on the spectral energy distributions we are not able to distinguish between X-ray-heated or viscously-heated disk spectra. NIR/X-ray flux correlations could in principle be used to shed more light this. Russell et al. (2007) used such correlations for a large ensemble of NSXBs that covered more than five decades in X-ray luminosity. Although our X-ray observations of 4U 1705−440 only span about a decade in X-ray luminosity, a clear correlation between X-ray and nIR fluxes can be seen in Figure 5. The best-fit power-law slope of 0.66±0.02 is consistent with that found for the large sample of NSXB, which did not include 4U 1705−440, and also consistent with the expected slope from X-ray heating (Russell et al. 2007). A viscously-heated disk would have resulted in a slope of ∼0.3. Russell et al. (2007) combined the NSXB data regardless of spectral state. Dividing our data based on the dominant X-ray spectral component (thermal vs. non-thermal) reveals a significantly steeper relation for the (hard) non-thermal X-ray state than for the (soft) thermal X-ray state (see Figure 5): 1.33±0.11 compared to 0.37±0.03. Although these different slopes are obtained from small numbers of points, they are both no longer consistent with X-ray heating. The slope for the (soft) thermal state is marginally consistent with viscous heating, while the slope for the (hard) non-thermal state is similar to that found between radio flux and X-ray flux in NSXBs, $L_{radio} \propto {L_X}^{1.4}$ (Migliari & Fender 2006). For this slope also to be observed

in the nIR, the nIR-radio spectral index would have to be very flat, requiring the nIR to originate from the optically-thick part of a jet synchrotron spectrum, for which we see no evidence however.

An additional test to distinguish between X-ray and viscous heating is to search for lags between changes in the nIR and X-ray emission of a few days or more. Such lags are not expected when X-ray heating is important, as reprocessing of the X-rays is near-instantaneous. If, on the other hand, X-ray heating is not important, variations in the X-rays from the inner disk will lag variations in the nIR emission from the non-irradiated outer disk, since changes in the mass-accretion rate travel through the disk on the viscous time scale. Such delays have been observed in GX 339-4 for example (Homan et al. 2005), where a lag time of 15–20 days was measured. In Figure 8 we plot the broadband X-ray flux of the thermal component (disk and boundary layer; filled dots), the non-thermal power-law component (open squares), and the K_s flux density light curves from an X-ray flux cycle in 2007 July-September that was sampled well in the nIR. The result is ambiguous, mainly because the source underwent a spectral transition in X-rays, making it hard to follow the disk component over a long period of time; changes in the disk X-ray flux during a transition probably do not only reflect changes in the mass-accretion rate through the inner disk. However, the figure does show that the nIR light curve resembles that of the total X-ray flux (thermal and non-thermal combined), suggesting the nIR flux is produced by X-ray heating. Better sampled light curves would be needed to perform a more detailed study of time lags.

Based on observed spectral indices Russell et al. (2007) concluded that in atoll NSXBs with 2–10 keV luminosities above 10^{36} erg s^{-1} jet emission dominates the nIR. Distance estimates from radius expansion bursts (7.2–9.6 kpc Jonker & Nelemans 2004; Galloway et al. 2006), indicate that the 2–10 keV luminosity of 4U 1705−440 is well above this value. However, our spectral indices are more consistent with disk emission. The observed 0.5–100 keV flux range of 4U 1705−440 leads to a total luminosity range of $0.7 - 14.9 \times 10^{37}$ erg s^{-1} (7.2 kpc) or $1.2 - 26.5 \times 10^{37}$ (9.6 kpc). These values are quite high for atoll sources and come close to those of the Z sources, possibly indicating a larger accretion disk than is typical for atoll sources. This could then explain why X-ray heating dominates the nIR in 4U 1705−440.

We conclude that X-ray heating of the outer disk and secondary star is the most likely source of the nIR emission in 4U 1705−440. Detection of possible orbital modulations and obtaining a nIR spectrum might help in distinguishing the relative importance of these two mechanisms. More observations are needed to study a possible X-ray state dependence of the nIR/X-ray relation.

We thank the numerous observers who have helped us obtain data: F. Baganoff, J.A. Black-

burne, A. Burgasser, H.-W. Chen, D. Erb, S. Laycock, S. Rappaport, P. Schechter, and M. Torres. Partial support for DLK was provided by NASA through Hubble Fellowship grant #01207.01-A awarded by the Space Telescope Science Institute, which is operated by the Association of Universities for Research in Astronomy, Inc., for NASA, under contract NAS 5-26555. PyRAF is a product of the Space Telescope Science Institute, which is operated by AURA for NASA. This research has made use of data obtained from the High Energy Astrophysics Science Archive Research Center (HEASARC), provided by NASA's Goddard Space Flight Center.

Facilities: Magellan:Baade (PANIC), CTIO:Blanco (ISPI)

REFERENCES

Arnaud, K. A. 1996, in ASP Conf. Ser. 101: Astronomical Data Analysis Software and Systems V, Vol. 5, 17

Barret, D. & Olive, J. 2002, ApJ, 576, 391

Barthelmy, S. D., Barbier, L. M., Cummings, J. R., et al. 2005, Space Science Reviews, 120, 143

Bertin, E. & Arnouts, S. 1996, A&AS, 117, 393

Bessell, M. S. 1991, AJ, 101, 662

Bessell, M. S. & Brett, J. M. 1988, PASP, 100, 1134

Buxton, M. & Bailyn, C. 2004, ApJ, in press

Cardelli, J. A., Clayton, G. C., & Mathis, J. S. 1989, ApJ, 345, 245

Carroll, B. W. & Ostlie, D. A. 1996, An introduction to modern astrophysics (Reading, MA: Addison-Wesley, —c1996)

di Salvo, T., Iaria, R., Méndez, M., et al. 2005, ApJ, 623, L121

Dutra, C. M., Santiago, B. X., & Bica, E. 2002, A&A, 381, 219

Fender, R. 2006, Jets from X-ray binaries (Compact stellar X-ray sources), 381–419

Ford, E. C., van der Klis, M., & Kaaret, P. 1998, ApJ, 498, L41

Frank, J., King, A., & Raine, D. 1992, Accretion Power in Astrophysics (Accretion Power in Astrophysics, ISBN 0521408636, Cambridge University Press, 1992.)

Galloway, D. K., Muno, M. P., Hartman, J. M., et al. 2006, astro-ph/0608259

Giacconi, R., Murray, S., Gursky, H., et al. 1972, ApJ, 178, 281

Gottwald, M., Haberl, F., Langmeier, A., et al. 1989, ApJ, 339, 1044

Hasinger, G. & van der Klis, M. 1989, A&A, 225, 79

Homan, J., Buxton, M., Markoff, S., et al. 2005, ApJ, 624, 295

Jahoda, K., Markwardt, C. B., Radeva, Y., et al. 2006, ApJS, 163, 401

Jonker, P. G. & Nelemans, G. 2004, MNRAS, 354, 355

Levine, A. M., Bradt, H., Cui, W., et al. 1996, ApJ, 469, L33

Lin, D., Remillard, R. A., & Homan, J. 2007, ApJ, 667, 1073

Martini, P., Persson, S. E., Murphy, D. C., et al. 2004, Proc. SPIE, 5492, 1653, (astro-ph/0406666)

Migliari, S. & Fender, R. P. 2006, MNRAS, 366, 79

Migliari, S., Tomsick, J. A., Maccarone, T. J., et al. 2006, ApJ, 643, L41

Mikami, T. & Heck, A. 1982, PASJ, 34, 529

Olive, J.-F., Barret, D., & Gierliński, M. 2003, ApJ, 583, 416

Piraino, S., Santangelo, A., di Salvo, T., et al. 2007, A&A, 471, L17

Predehl, P. & Schmitt, J. H. M. M. 1995, A&A, 293, 889

Reig, P., Papadakis, I., & Kylafis, N. D. 2003, A&A, 398, 1103

Rothschild, R. E., Blanco, P. R., Gruber, D. E., et al. 1998, ApJ, 496, 538

Russell, D. M., Fender, R. P., Hynes, R. I., et al. 2006, MNRAS, 371, 1334

Russell, D. M., Fender, R. P., & Jonker, P. G. 2007, MNRAS, 379, 1108

Skrutskie, M. F., Cutri, R. M., Stiening, R., et al. 2006, AJ, 131, 1163

Sztajno, M., Langmeier, A., Frank, J., et al. 1985, IAU Circ., 4111, 1

van der Klis, M. 2006, in Compact stellar X-ray sources (Cambridge, UK: Cambridge University Press, 2006 Cambridge astrophysics series, Vol. 39, edited by Walter H.G. Lewin and Michiel Van der Klis, p. 39)

Vrtilek, S. D., Raymond, J. C., Garcia, M. R., et al. 1990, A&A, 235, 162

Zurita, C., Casares, J., Shahbaz, T., et al. 2000, MNRAS, 316, 137

Table 1. Near-IR Observation Summary for 4U 1705−440

Epoch	Date†	K_s				H				J			
		Time	Exp. (s)	Airmass	Seeing	Time	Exp. (s)	Airmass	Seeing	Time	Exp. (s)	Airmass	Seeing
1	2006-May-16	06:06	50	1.04	0.6	06:22	240	1.04	0.7	06:11	450	1.04	0.7
2	2006-Jul-15	00:34	230	1.12	0.7	00:47	1296	1.10	0.7	01:19	1620	1.07	0.7
3	2006-Aug-04	00:45	180	1.04	0.6	00:51	864	1.04	0.7	01:18	1620	1.04	0.7
4	2006-Aug-08a	00:45	90	1.04	0.9	00:07	432	1.05	1.1	00:20	810	1.04	0.9
5	2006-Aug-08b	23:47	180	1.06	1.0	23:54	432	1.06	1.0	00:06	1215	1.05	1.0
6	2006-Aug-09	23:37	90	1.07	0.7	23:43	432	1.06	0.8	23:55	810	1.05	0.9
7	2006-Aug-26	23:30	270	1.04	0.7	23:53	1296	1.04	0.7	00:35	2430	1.06	0.8
8	2007-Apr-07	09:42	100	1.05	0.6	···	···	···	···	09:35	100	1.04	0.6
9	2007-May-09	07:56	300	1.06	0.7	···	···	···	···	···	···	···	···
10	2007-Jul-05	01:08	200	1.16	0.8	···	···	···	···	01:31	200	1.12	0.7
11⋆ ..	2007-Jul-24	01:53	320	1.03	1.0	···	···	···	···	···	···	···	···
12⋆ ..	2007-Jul-27	06:31	480	1.96	0.8	···	···	···	···	···	···	···	···
13	2007-Jul-31a	01:45	90	1.04	0.7	01:36	270	1.04	0.7	01:27	270	1.04	0.7
14	2007-Jul-31b	23:25	110	1.16	0.7	···	···	···	···	23:34	270	1.14	0.7
15	2007-Aug-03	02:06	300	1.04	0.6	···	···	···	···	···	···	···	···
16	2007-Aug-20	00:51	180	1.04	0.6	···	···	···	···	01:01	360	1.04	0.5
17	2007-Sep-01	02:46	220	1.30	0.4	···	···	···	···	···	···	···	···
18	2007-Sep-22	01:38	360	1.35	0.8	01:29	450	1.32	0.7	01:23	180	1.30	0.9

†All dates and times are UT.

⋆All observations were done with Baade/PANIC, except for these which used Blanco/ISPI.

Table 2. Photometry of 4U 1705−440

Epoch	X-ray state	Magnitude		
		K_s	H	J
1	Soft	15.23 ± 0.02	16.03 ± 0.02	17.14 ± 0.02
2	?⋆	16.18 ± 0.02	16.82 ± 0.02	17.96 ± 0.02
3	?⋆	16.10 ± 0.02	16.93 ± 0.02	18.16 ± 0.02
4	Hard	16.98 ± 0.08	17.41 ± 0.03	18.47 ± 0.03
5	Hard	16.74 ± 0.03	17.37 ± 0.03	18.39 ± 0.03
6	Hard	16.83 ± 0.03	17.42 ± 0.03	18.48 ± 0.03
7	Hard	16.66 ± 0.02	17.34 ± 0.02	18.39 ± 0.02
8	Soft	15.51 ± 0.02	···	17.05 ± 0.02
9	Soft	15.77 ± 0.02	···	···
10	Soft	16.19 ± 0.02	···	17.94 ± 0.03
11	Hard	17.25 ± 0.07	···	···
12	Hard	17.10 ± 0.06	···	···
13	Hard	16.41 ± 0.03	16.94 ± 0.02	18.01 ± 0.02
14	Hard	16.54 ± 0.03	···	18.23 ± 0.03
15	Hard	16.31 ± 0.02	···	···
16	Soft	15.61 ± 0.02	···	17.10 ± 0.02
17	Soft	15.37 ± 0.02	···	···
18	Soft	15.60 ± 0.02	16.18 ± 0.02	17.14 ± 0.02

⋆The state identification of these two observations is uncertain.

Note. — The quoted errors only reflect `sextractor` uncertainties. Additional uncertainties related to flat fielding and sky subtraction are estimated to be 0.05 mag.

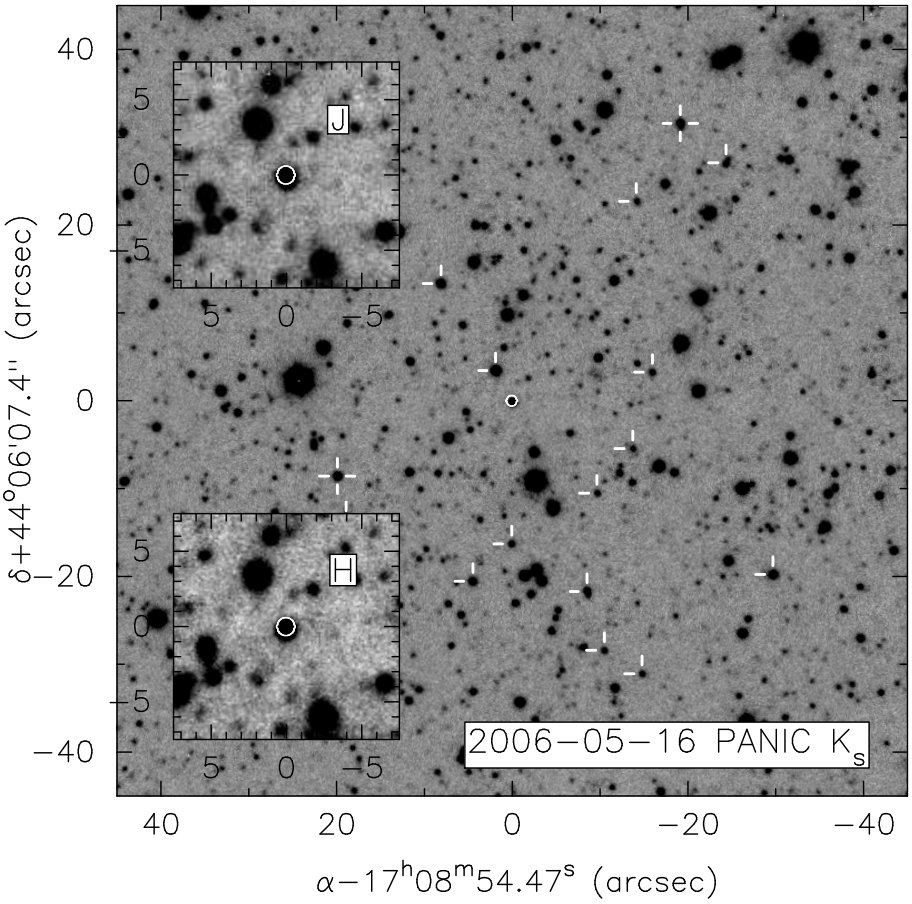

Fig. 1.— Images of the field around 4U 1705−440 from the 2006 May 16 PANIC observation. The main panel shows a 1.′5 × 1.′5 field of the K_s image. The *Chandra* position of 4U 1705−440 is marked with a 0.″6-radius circle. We also indicate with tick marks a number of the photometric reference stars (some are hidden behind the sub-panels or are off this image): the two most stable stars have crosses, while the rest have only ticks to the north and east. The sub-panels show 15″ × 15″ fields of the J (top left) and H (bottom left) images. North is up, and east to the left.

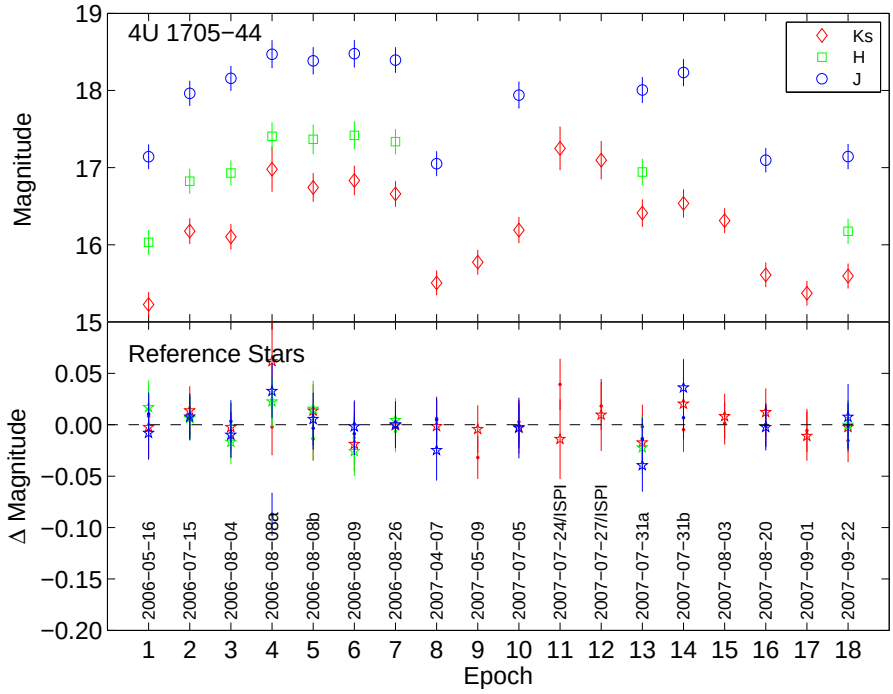

Fig. 2.— Photometry of 4U 1705−440. In the top panel we show the K_s (diamonds), H (squares), and J (circles) photometry of 4U 1705−440 plotted as a function of epoch number. In the bottom panel we show the variation in the magnitudes of the two most stable reference stars (see Fig. 1). The colors/gray-scales represent the same filters, but here the two symbols (points and stars) correspond to the two reference stars. The date of each epoch is listed in the bottom panel. [*(See the electronic edition of the Journal for a color version of this figure.*]

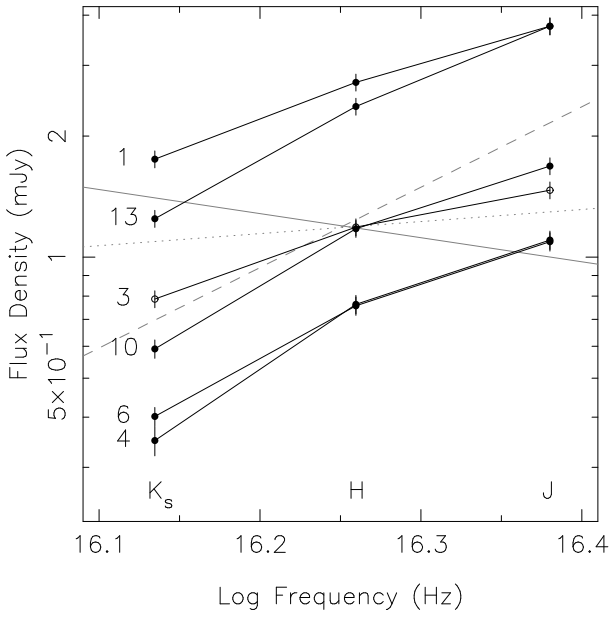

Fig. 3.— Six representative nIR spectral energy distributions (SEDs) of 4U 1705−440, dereddened assuming an N_H of $1.9{\times}10^{22}$ atoms cm^{-2} ($A_V = 10.3$). The nIR epoch of each of the SEDs is shown on the left-side of the K_s data points. The solid grey line depicts a typical optically thin synchrotron spectrum from a jet ($\propto \nu^{-0.6}$). The dashed line represents the Rayleigh-Jeans tail of the spectrum of a viscously heated accretion disk ($\propto \nu^2$) and the dotted line the shallower 'stretched' part that is characteristic of such a disk spectrum ($\propto \nu^{1/3}$).

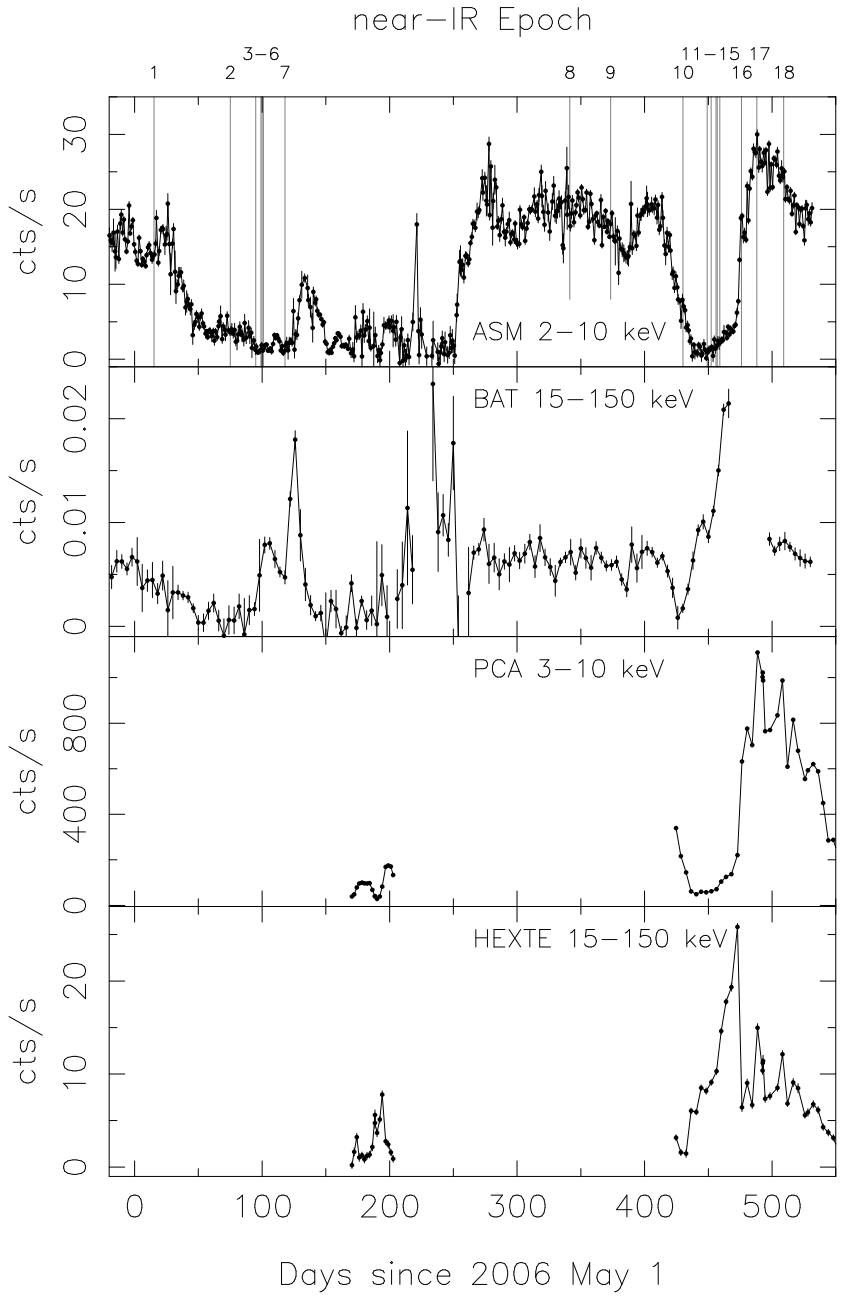

Fig. 4.— X-ray light curves of 4U 1705−440 from various instruments. From top to bottom: *RXTE*/ASM, *Swift*/BAT, *RXTE*/PCA, and *RXTE*/HEXTE. The ASM and BAT light curves show one- and four-day averages, respectively, whereas the PCA and HEXTE light curves were rebinned to one data point per observation. The times of the nIR observations are indicated by the vertical lines and numbers in and above the top panel.

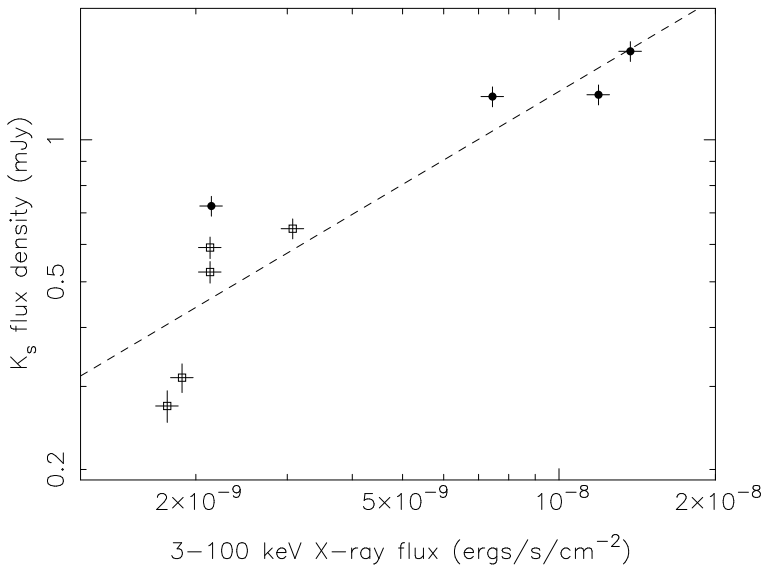

Fig. 5.— K_s flux density versus unabsorbed X-ray flux (3–100 keV). The dashed line shows the best power-law fit to the data with an index of 0.66(2). Filled circles correspond to observations in which the thermal components dominates the X-ray spectrum ($> 85\%$), open squares ones in which the non-thermal flux dominates ($> 75\%$).

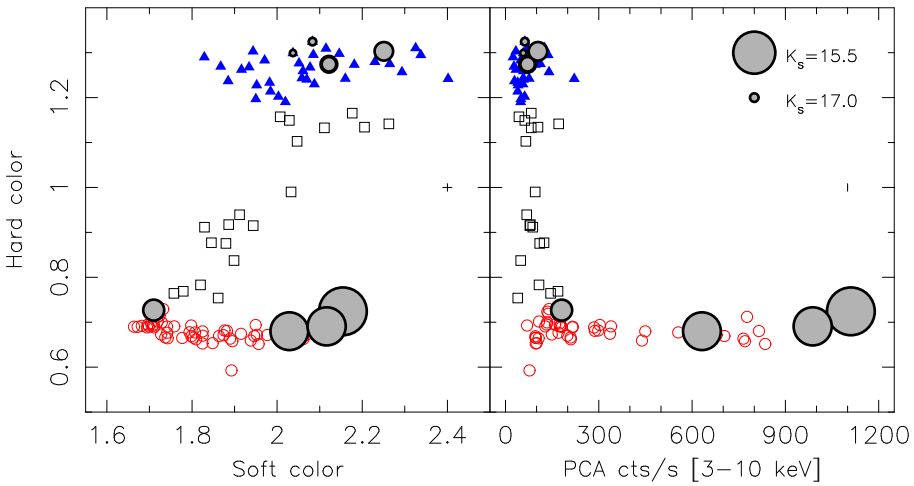

Fig. 6.— Color-color (left) and color-count rate diagrams (right) of 4U 1705−440, created from *RXTE*/PCA data. Soft color and hard color were defined as count rate ratios in the bands (4.0–7.3 keV)/(2.3–4.0 keV) and (9.8–18.2 keV)/(7.3–9.8 keV), respectively. Typical error bars are shown on the right hand side of each panel. Triangles, squares, and open circles indicate the spectrally hard ("extreme island"), transitional ("island"), and soft ("banana") states, respectively. The gray circles depict observations coincident (within two days) with our nIR observations, with the size of the circles scaling linearly with nIR flux density. [*(See the electronic edition of the Journal for a color version of this figure.*]

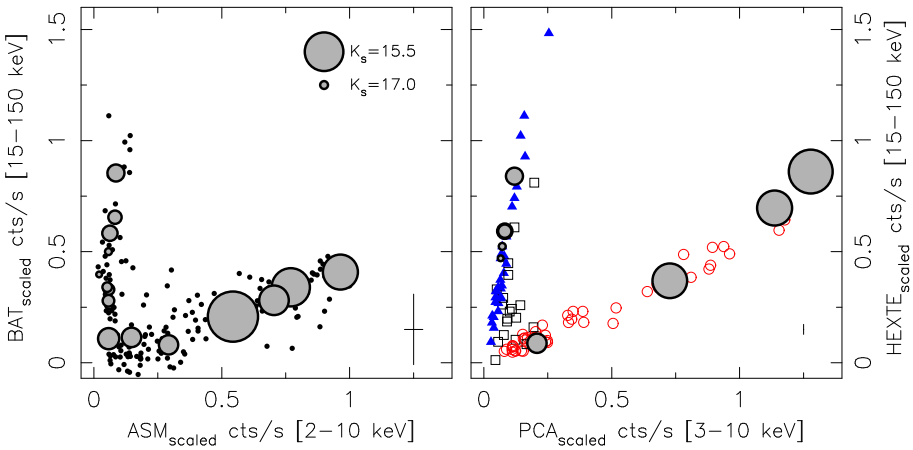

Fig. 7.— High-energy versus low-energy scaled count rates from ASM/BAT (left) and PCA/HEXTE (right). The count rates were scaled as described in §3.2. Typical error bars are shown in the lower right corner of each panel. Triangles, squares, and open circles in the right panel indicate the spectrally hard ("extreme island"), transitional ("island"), and soft ("banana") states, respectively. The gray circles depict observations coincident (within two days) with our nIR observations, with the size of the circles scaling linearly with nIR flux density. [*(See the electronic edition of the Journal for a color version of this figure.*]

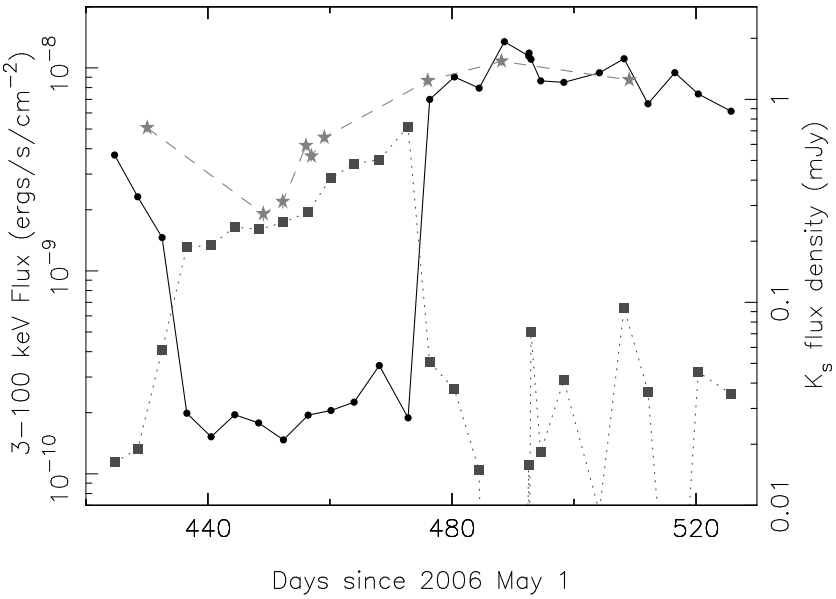

Fig. 8.— Comparison of thermal (dots) and non-thermal (squares) X-ray light curves (3–100 keV) and K_s-band (stars) light curves during a transition cycle in July-September 2007.